View Online / Journal Homepage
Dynamic Article Links

Lab on a Chip

Cite this: DOI: 10.1039/c2lc21045b

www.rsc.org/loc

PAPER

Cell separation based on size and deformability using microfluidic funnel ratchets

Sarah M. McFaul,[a] Bill K. Lin[a] and Hongshen Ma*[abc]

Received 28th October 2011, Accepted 16th March 2012
DOI: 10.1039/c2lc21045b

The separation of biological cells by filtration through microstructured constrictions is limited by unpredictable variations of the filter hydrodynamic resistance as cells accumulate in the microstructure. Applying a reverse flow to unclog the filter will undo the separation and reduce filter selectivity because of the reversibility of low-Reynolds number flow. We introduce a microfluidic structural ratchet mechanism to separate cells using oscillatory flow. Using model cells and microparticles, we confirmed the ability of this mechanism to sort and separate cells and particles based on size and deformability. We further demonstrate that the spatial distribution of cells after sorting is repeatable and that the separation process is irreversible. This mechanism can be applied generally to separate cells that differ based on size and deformability.

Introduction

The separation of individual populations of cells from heterogeneous samples without chemical modification or labelling is important in many areas in medicine and biology.[1–4] Current approaches can be broadly divided into hydrodynamic techniques[5–8] that use flow around micro-scale obstacles to selectively direct cells into different streams, and filtration techniques that use arrays of micro-scale constrictions or pores to selectively trap cells.[9–16] Hydrodynamic techniques primarily separate cells based on size, whereas filtration techniques can separate cells based on size and deformability. This capability is particularly interesting since deformability is often more strongly correlated with different cell phenotypes.[17,18] The selectivity of filtration separation techniques, however, is limited by clogging. As cells become lodged in the filter microstructure, the overall hydrodynamic resistance (R_H) of the filter changes and diminishes the effect of the applied pressure gradient in an unpredictable manner,[19] as shown in Fig. 1. The selectivity of traditional filtration is further limited by cytoskeleton remodelling, whereby a persistent force wedging cells into the filter induces changes in the internal structure of the cell,[20] enabling some trapped cells to gain passage over time. Furthermore, prolonged contact between the cells and the filter surface increases the potential for non-specific adsorption, which exacerbates clogging and prevents the recovery of the cells after separation.[19]

The lack of selectivity caused by clogging may be addressed by periodically removing cells that accumulate in the filter microstructure to reset the hydrodynamic resistance of the filter to its initial value. Crossflow filters attempt to do so by adding a perpendicular component to the filtration. However, current devices show limited selectivity because the presence of the perpendicular flow disrupts the ability to produce consistent deformation forces across the filtration microstructures.[21,22] Another approach to remove clogged cells is to periodically introduce a reverse-flow through the filter.[23] The effectiveness of this remedy is also limited because the reversibility of inertia-less, low-Reynolds number flow will undo the initial separation. Furthermore, the cleared cells will re-accumulate in the filter microstructure immediately following the flow reversal step in the next filtration cycle. Flow reversibility in low-Reynolds number systems can be countered using a ratchet mechanism, such as those that have been developed using thermal

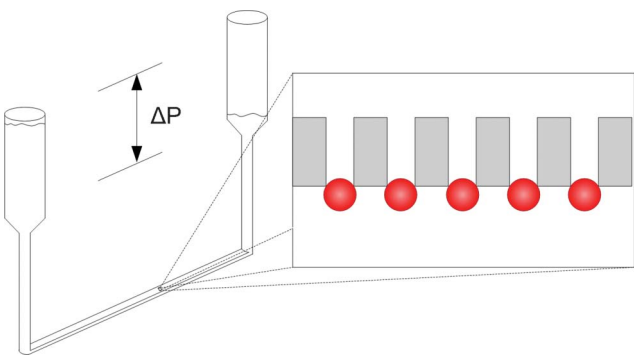

Fig. 1 Cell clogging in a traditional filtration mechanism. As cells block the pores of the microstructure, the hydrodynamic resistance of the filter changes unpredictably.

[a]*Department of Mechanical Engineering, University of British Columbia, 2054-6250 Applied Science Lane, Vancouver, BC, Canada V6T 1Z4. E-mail: hongma@mech.ubc.ca; Tel: +1 604-827-4703*
[b]*Department of Urologic Science, University of British Columbia, Level 6, 2775 Laurel Street, Vancouver, BC, Canada V5Z 1M9*
[c]*Vancouver Prostate Centre, Vancouver General Hospital, 2660 Oak Street, Vancouver, BC, Canada V6G 3Z6*

gradients,[24] electromagnetic fields,[25] physical geometry,[26–28] and various combinations thereof.[29,30] However, these mechanisms have only presented the possibility of separating particles based on size, but not deformability.

Previously, we proved the existence of a structural microfluidic ratchet created using funnel-shaped micrometre-scale constrictions and demonstrated unidirectional transport of single cells when the carrier fluid is subjected to an unbiased oscillatory flow.[31] The funnel microstructures are sized such that the entrance side of the funnel is larger than the diameter of the cells, while the exit side is smaller than the diameter of the cells. The pressure required to deform single cells through such a constriction along the direction of the taper is less than the pressure required against the direction of the taper. When a cell is deformed into a constriction, the pressure required to advance the position of the cell increases until a point of instability, known as Haines' jump, where the cell is rapidly pulled through the constriction.[32] The threshold pressure for Haines' jump depends on the radius of the leading cell surface and the radius of the following cell surface, which are in turn determined by the geometrical constraint provided by the funnel taper.

In this paper, we leverage this ratchet effect to create a physical cell separation device where cell samples are transported through a matrix of funnel constrictions using an oscillatory flow. The small and deformable cells transit through the constrictions in forward flow, while the large and rigid cells are blocked (Fig. 2A). When the flow direction is reversed to unclog the constrictions, small and deformable cells are unable to pass back through (Fig. 2B). Using multiple linear arrays of these constrictions enables cell sorting based on size and deformability. We describe the design of this mechanism along with supporting microfluidic circuitry to generate the flow conditions necessary for reliable cell sorting and separation. We further characterize the selectivity of the device using model cells, study the relative contributions of cell deformability *versus* cell size, determine the effect of various device parameters, and confirm the irreversibility of the sorted cell population.

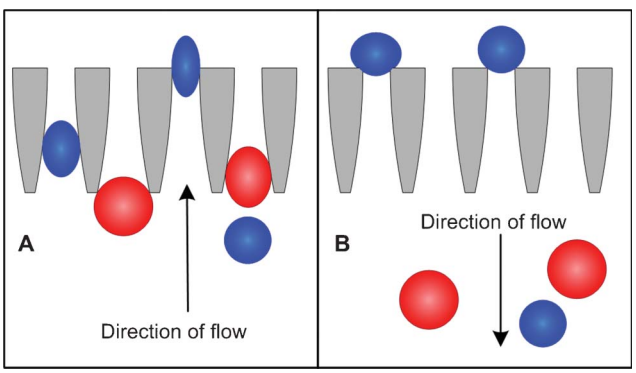

Fig. 2 Microfluidic ratchet cell sorting mechanism. (A) Smaller and more deformable cells can squeeze through funnel constrictions in forward flow while larger less deformable cells are excluded. (B) Smaller more deformable cells are unable to pass back through the funnel constrictions when flow direction is reversed to unclog the filter.

Design

Funnel shape design

Key design parameters of the funnel microstructures include pore size, channel depth, and shape of the funnel taper. The pore size of the funnel is defined as the narrowest portion of the constriction and is varied depending on the funnel's location within the sorting area. The depth of the microstructure is 25 μm, which accommodates typical mammalian cells in suspension. The shape of the funnel taper directly affects the pressure asymmetry. By considering the cell as a liquid drop with a constant cortical tension (T_c), the threshold pressure can be modeled using a version of the Laplace–Young equation:

$$\Delta P = T_c\left(\frac{1}{R_a} - \frac{1}{R_b}\right) \quad (1)$$

The leading and trailing radii (R_a and R_b in Fig. 3) are determined by the funnel geometry using volume conservation. We developed a numerical model of the expected pressure asymmetry for 50 μm long funnels of various geometries with rectangular cross sections. Specifically, we looked at straight tapers of the form $y = \pm(mx + W_0)$ and parabolic tapers of the form $y = \pm(kx^2 + W_0)$. Expectedly, more gradual tapers, as defined by smaller k and m values, result in greater asymmetries. However, these more gradual shapes also increase the length for which the cell is in contact with the funnel walls, leading to increased risk of clogging or cell damage. Furthermore, parabolic tapers yielded greater directional asymmetry at smaller cell compression levels, allowing ratcheting to be enabled at smaller pressures. To balance these considerations, we chose a parabolic funnel shape with $k = 2000\ m^{-1}$. Table 1 shows the calculated pressure asymmetry for a 10 μm diameter cell being deformed through 3 parabolic and 3 linear tapers at various compression levels.

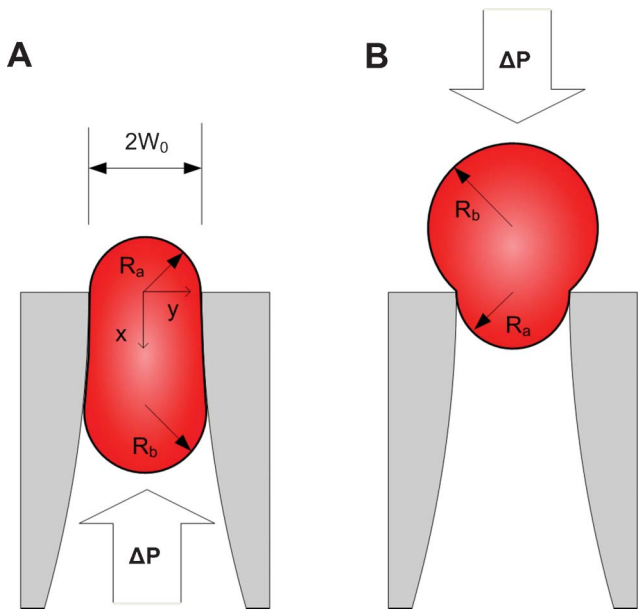

Fig. 3 Model of cell deformation through a tapered constriction in the forward (A) and reverse (B) directions.

Table 1 Asymmetry of the deformation pressure as predicted using the liquid-drop model for a 10 μm diameter cell deformed through various linear and parabolic constrictions. Results are shown for funnel constrictions that diametrically deform the cell from 5 to 20%

		Maximum diametrical deformation of 10 μm diameter cell			
		5%	10%	15%	20%
Parabolic tapers	$k = 1000\ m^{-1}$	1.5	3.4	5.0	5.9
	$k = 2000\ m^{-1}$	1	2.4	3.5	4.2
	$k = 3000\ m^{-1}$	1	2.0	2.9	3.4
Straight tapers	$m = 0.035$	1	2.1	3.1	3.9
	$m = 0.087$	1	1	1.4	1.7
	$m = 0.176$	1	1	1	1

Cell sorting funnel array

The cell sorting microstructures consist of funnel constrictions arranged in a 2D array with 12 rows and 128 funnels in each row. Detailed dimensions of the funnel microstructures are shown in Fig. 4A. A schematic of the cell separation area is shown in Fig. 4B. The funnel pore size is constant in each row, but decreases with each successive row in increments of 1 μm from 15 to 4 μm in one design and from 12 to 2 μm in another. The designs of these two devices are otherwise identical. The funnel constrictions are aligned vertically to one another in order to maintain a linear streamline from one row to the next during the sorting process. A cell suspension is pushed through the funnel array using a planar flow with uniform flow profile across the 128 funnels. A uniform flow profile is important to ensure that the carrier fluid delivers a similar hydrodynamic force to each cell. The uniform flow profile is generated using a tree microchannel network where a single stream is repeatedly bifurcated into 128 identical streams. Membrane microvalves,[33] V1 to V6 in Fig. 4C, are used to create precisely controlled flows through the funnel array in the horizontal direction for infusion and extraction, as well as in the vertical direction for separation.

The separation process, shown in Fig. 4B, involves initially infusing the cell sample below the first row of funnels using a horizontal flow by opening valves V1 and V2 while sealing V3 through V6. The sample is then sorted using the microfluidic ratchet mechanism by applying an oscillatory flow in the vertical direction, which is generated using a fluidic H-bridge created by valves V3 through V6 to switch on/off the forward and reverse pressure. Specifically, during the forward flow phase, V5 and V6 are opened, while V3 and V4 are closed. During the reverse flow phase, the states of these valves are inverted. Finally, the separated cells are extracted using a horizontal flow from a buffer inlet with valves configured as the infusion process. This cycle can be repeated indefinitely to increase the throughput of the separation process.

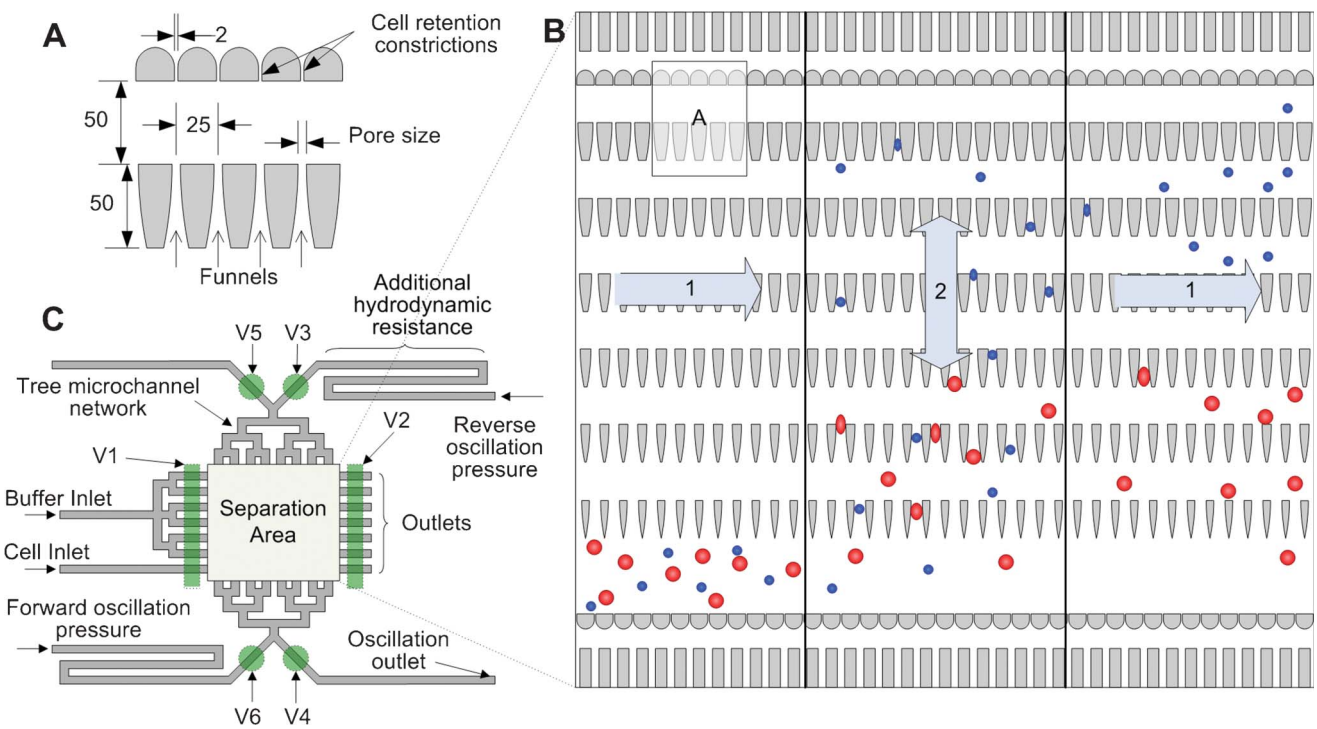

Fig. 4 Device design schematic. (A) Detailed design of the funnel and cell retention microstructures with dimensions shown in micrometres. (B) Schematic of the cell separation area within the device illustrating the inflow/outflow phase (1) and separation phase (2). (C) Overview of device layout showing inlets, outlets, and valves (V1 to V6).

Cell retention

To prevent cells from entering the tree microchannel network, an array of 2 μm constrictions is added between the tree networks and the funnel array (Fig. 4A). The blocks between these constrictions have a semicircular shape on one side to enhance the manufacturability of these structures in photolithographic microfabrication.

Precision flow control

The flow velocity of the streamlines in the funnel array is controlled using an elongated microchannel in series with the tree microchannel network. This microchannel provides a dominant hydrodynamic resistance that dictates the fluid flow resulting from the pressure applied between the oscillation pressure inlet and the oscillation outlet in Fig. 4C. The geometry of this microchannel (100 μm wide × 25 μm tall × 32 800 μm long) is designed to generate a target flow rate on the order of 100 μm s^{-1} in the funnel array region based on an oscillatory pressure amplitude of 3.5 kPa according to the following formula:

$$R_H = \frac{\Delta P}{Q} \quad (2)$$

R_H is the hydrodynamic resistance, ΔP the pressure drop, and Q the volumetric flow rate. For a rectangular channel in laminar flow, the hydrodynamic resistance can be calculated using:

$$R_H \approx \frac{12\mu L}{wh^3} \quad (3)$$

where μ is the viscosity of the fluid; L, w, and h are the length, width, and depth of the channel; and $w > h$.

Materials and methods

Fabrication of silicon masters

Patterns of the required microstructures are drawn using Solidworks DWG-Editor to generate commercially-produced optical photomasks. Inverse versions of the required microstructures are fabricated on a silicon wafer using two photolithographic steps. First, the silicon wafer is coated with a layer of SU-8 negative photoresist (Microchem) and spun at a speed of 1200 rpm for 50 s. This wafer is baked on a 95 °C hotplate for 5 minutes and then exposed to UV light through the first optical photomask (Advance Reproductions, Andover, MA, USA). The wafer is then baked at 65, 95, then 65 °C for 1, 4, and 1 minutes respectively. The patterned wafer is developed using SU-8 developer (Microchem) and washed with isopropanol. To harden the patterned microstructures, the wafer is baked at 200 °C for one hour. This final bake temperature is reached by a slow ramp at a rate of 10 °C every 12 minutes. After baking, the wafer is allowed to equilibrate to room temperature on top of the hotplate. SPR220-7.0 photoresist (Microchem) is used to create structures for microvalves on the device. This photoresist is added to the cooled wafer by spin coating at 600 rpm for 50 s. The edge bead is removed from the wafer manually and then softbaked for 1, 5, and 1 minutes at 65, 95, and 65 °C respectively. A second photomask (CAD/Art Services, Brandon, OR, USA) is aligned to the previous set of patterns and subsequently exposed and developed in MF 319 developer (Microchem). Finally, the wafer is baked on a hotplate at 95 °C for 5 minutes to allow the SPR220-7.0 photoresist layer to reflow and take on a parabolic profile. Great care is taken throughout the process to prevent exposing the wafer to thermal shocks, which can cause the micro-scale SU-8 features to warp and bend. The fluid control layer is fabricated on a second silicon wafer using a single layer of SPR 220-7.0 using the same procedure as described above.

Fabrication of PDMS devices

The PDMS masters are fabricated using standard multi-layer soft lithography techniques.[33] The flow layer is formed using a 5 : 1 base to hardener ratio of RTV 615 silicone (Momentive Performance Materials), while the flow layer is formed using a 20 : 1 ratio. The flow and control layers are bonded together by diffusion. The bonded flow and control layer is subsequently attached to a glass slide following 45 s activation in air plasma (Harrick Plasma, Ithaca, NY, USA). Inlets and outlets are punched manually using a 0.5 mm punch (Technical Innovations, Angelton, TX, USA).

Sample preparation

Cell sorting experiments were conducted using peripheral blood mononuclear cells (PBMCs), L1210 mouse lymphoma cells (MLCs), and microparticles. Peripheral blood mononuclear cells were prepared from whole blood obtained from healthy volunteers. Whole blood was drawn into 6 ml sodium heparin containing tubes. PBMCs were separated out using Histopaque 1077 (Sigma-Aldrich) according to the manufacturer's instructions, and then re-suspended at a concentration of 1 × 10^7 cells ml^{-1} in AIM 5 media (GIBCO-Invitrogen). MLCs were cultured in suspension using RPMI 1640 (Gibco, Invitrogen) with 10% fetal bovine serum and 1% penicillin/streptomycin. These cells were incubated at 37 °C with 100% humidity and 5% CO_2. Prior to experimentation, the cells were concentrated *via* centrifugation and re-suspended in a solution of phosphate buffered saline (PBS) containing 0.4% bovine serum albumin at a concentration of 1 × 10^7 cells ml^{-1}. Cells were used for experimentation between 3 to 4 days after passaging. In experiments where cells were stained, the L3224 LIVE/DEAD Viability/Cytotoxicity kit (Invitrogen) was used according to the manufacturer's directions. Microparticles of sizes 6.37 ± 0.48 μm and 10.14 ± 1.04 μm (Bangs Laboratories) were used for particle experiments. 50 μL of each were suspended in 1 ml of deionized water with 0.5% of Tween 20 (Invitrogen).

Experimental setup and preparation

Precise control of fluid flow in the device was achieved using a commercial pressure controller (Fluigent, Paris, France). Microvalves integrated in the PDMS microstructure were actuated using a custom-designed pressure controller described previously.[31] Cell distributions were determined by visual inspection using an inverted microscope (Nikon Ti-U) and CCD camera (Nikon DS-2MBW). Diameters of cells in suspension were measured using NIS Elements microscopy software (Nikon).

Prior to each experiment, a solution of 1% BSA in PBS was used to fill the device prior to operation and incubated for

10 minutes to prevent nonspecific adsorption of cells onto the PDMS surface. The device was then flushed with PBS. To load cells into the separation area, a pressure of 2 kPa was applied to both the cell and buffer inlets simultaneously. Equal oscillation pressures were applied to both the upper and lower oscillation inlets and ranged from 7 to 51 kPa.

Results and discussion

Cell sorting

To evaluate our separation mechanism, L1210 mouse lymphoma cells (MLCs) and human peripheral blood mononuclear cells (PBMCs) were used as mechanical models of two cell types with distinct mechanical properties. MLCs have diameters ranging from 8 to 14.5 μm with a mean of 11.1 μm and a standard deviation, σ_{size} = 1.2 μm. PBMCs have diameters ranging from 6 to 8.5 μm with a mean of 7.2 μm and σ_{size} = 0.6 μm. Cell deformability, as defined by cortical tension, was previously measured to be 413.6 ± 15.2 pN μm^{-1} and 35 pN μm^{-1} respectively for similar cell types.[34,35] Therefore, the deformability of L1210 MLCs is expected to be approximately 10 times that of PBMCs. For the purpose of device validation, PBMCs serve as a model of a smaller and more deformable cell, while MLCs serve as a model of a larger and more rigid cell.

Initially, each cell sample was separately infused into a device and sorted using an oscillatory pressure of 7 kPa. The timing of the oscillatory flow consisted of 3 s of forward pressure followed by 1 s of reverse pressure. The forward biased oscillation flow enables all cells to travel to a funnel constriction sufficiently small for ratcheting to occur. After 60 s of oscillation, the cells segregated in each row were counted manually using an optical microscope.

Both MLCs and PBMCs were observed to form consistent and narrow distributions in the matrix of funnel constrictions. The sorted MLC distribution had a mean of 9.7 μm and standard deviation of σ_{sorted} = 1.3 μm (Fig. 5A). The sorted PBMC distribution had a mean of 5.2 μm with σ_{sorted} = 1.2 μm (Fig. 5B). For MLCs, $\sigma_{sorted} \approx \sigma_{size}$, whereas for PBMCs, $\sigma_{sorted} \approx 2\sigma_{size}$. The broadening of the sorted PBMC distribution likely results from PBMCs being subjected to greater deformation relative to MLCs. Comparing the trapping constriction size with the cell size, the MLCs and PBMCs are compressed by an average of 13% and 28% respectively. Given the greater compression, the deformability of PBMCs likely made a greater contribution to the sorted distribution than size. Since more variation is typically associated with cell deformability than cell size, the resulting σ_{sorted} is broadened compared to σ_{size}.

To further investigate size *versus* deformability effects in the sorting process, we compared the distribution of MLCs with that of similarly sized polystyrene microparticles sorted under identical conditions. Microparticles (Bangs Laboratories, Fishers, IN) with diameters of 6.37 ± 0.48 μm and 10.14 ± 1.04 μm were mixed together to mimic the size range of MLCs. Since polystyrene microparticles are effectively incompressible relative to the polydimethylsiloxane (PDMS) structure, they can be considered to be sorted based on size alone. After sorting (oscillation pressure = 14 kPa), the diameters of both MLCs and microparticles were measured (measurement error = ±0.8 μm) as a function of their trapping funnel size (Fig. 5C). The microparticle sizes are strongly correlated to the trapping funnel size with a correlation coefficient of 0.93, whereas the corresponding property for MLCs showed a correlation coefficient of 0.65. The reduced correlation is a result of the variability in the deformability of the MLC population. For similarly sized cells and particles, the mean trapping funnel size differed by approximately 2 μm, which suggests that the cells are compressed by this amount on average during the sorting process. These results validate the potential to use our mechanism to sort cells and particles based on size and deformability, therefore expanding the current repertoire of separation methods.

To investigate changes in cell viability as a result of the sorting process, we stained a sample of MLCs using a live/dead assay. Since the possibility of compromising cell viability increases when higher pressures are applied to the cells, we evaluated cell viability over several oscillation pressures between 7 and 41 kPa. More than 95% of the sample cells were viable before and after sorting in each case.

Cell separation

To evaluate the ability of our device to separate cells from a mixture, we combined PBMCs with fluorescently stained MLCs

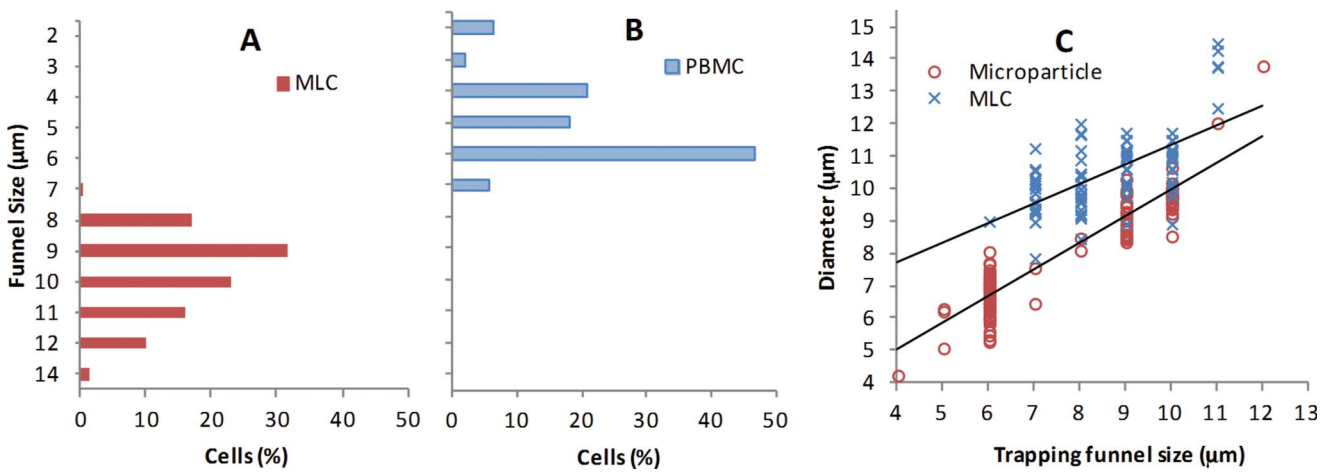

Fig. 5 Results from cell and particle sorting experiments. (A) Distribution of MLCs in the microfluidic funnel matrix after sorting. (B) Distribution of PBMCs. (C) Cell diameter *versus* trapping funnel size of sorted microparticles and MLCs with best-fit line drawn for both.

and sorted the sample under identical experimental conditions as described above. Example bright-field and fluorescence images and resulting distributions are shown in Fig. 6A–C. The distributions of MLCs and PBMCs overlapped in the 7 and 8 μm rows. Therefore, using the 8 μm pore as a cutoff yields a separation efficiency of 98% with a purity of 99% for the MLCs and correspondingly a 97% efficiency with 95% purity for the PBMCs in this sample (Fig. 6D). Efficiency and purity are defined as follows:

$$\text{Efficiency} = \frac{\text{Target cells in desired area}}{\text{Total target cells in sample}} \times 100\% \quad (4)$$

$$\text{Purity} = \frac{\text{Target cells in desired area}}{\text{Total cells in desired area}} \times 100\% \quad (5)$$

Device operating parameters

The mean and width of the cell distribution after sorting are primarily governed by three experimental parameters: the amplitude of the pressure oscillation, the timing of each oscillation cycle, and the total oscillation time. For most of these experiments, the standard operating conditions involved an oscillation pressure of 14 kPa, where each oscillation cycle consists of 3 s of forward pressure followed by 1 s of reverse pressure, applied for a total of 60 s.

The repeatability of this mechanism was evaluated over several sorting trials using MLCs under the aforementioned standard operating conditions. The trials were conducted on different days using devices from separate fabrication batches. As shown in Fig. 7A, the resulting distributions were consistent and repeatable. Specifically, the means and standard deviations of the distributions are within 6% and 12% of one another.

To study the effect of oscillation pressure, MLCs were sorted using pressures of 7, 14, 28, 41, and 55 kPa while all other parameters were kept constant. Expectedly, our results show an inverse relationship between the oscillation pressure and the mean of the resulting distribution (Fig. 7B). In addition, σ_{sorted} increased at higher oscillation pressures. Similarly to previous results obtained for PBMCs, more variance is associated with deformability than with size, and therefore the deformability-dominated sorting at higher pressures results in a wider distribution.

To evaluate the effect of oscillatory pressure timing, we sorted MLCs using forward pressure durations of 2, 3, 6, and 8 s, while keeping the reverse pressure duration at 1 s. The results show a thresholding effect where a minimum of 3 s is necessary for the sample cells to assume a characteristic distribution, while further increases in the period of the forward pressure do not lead to an altered steady-state distribution.

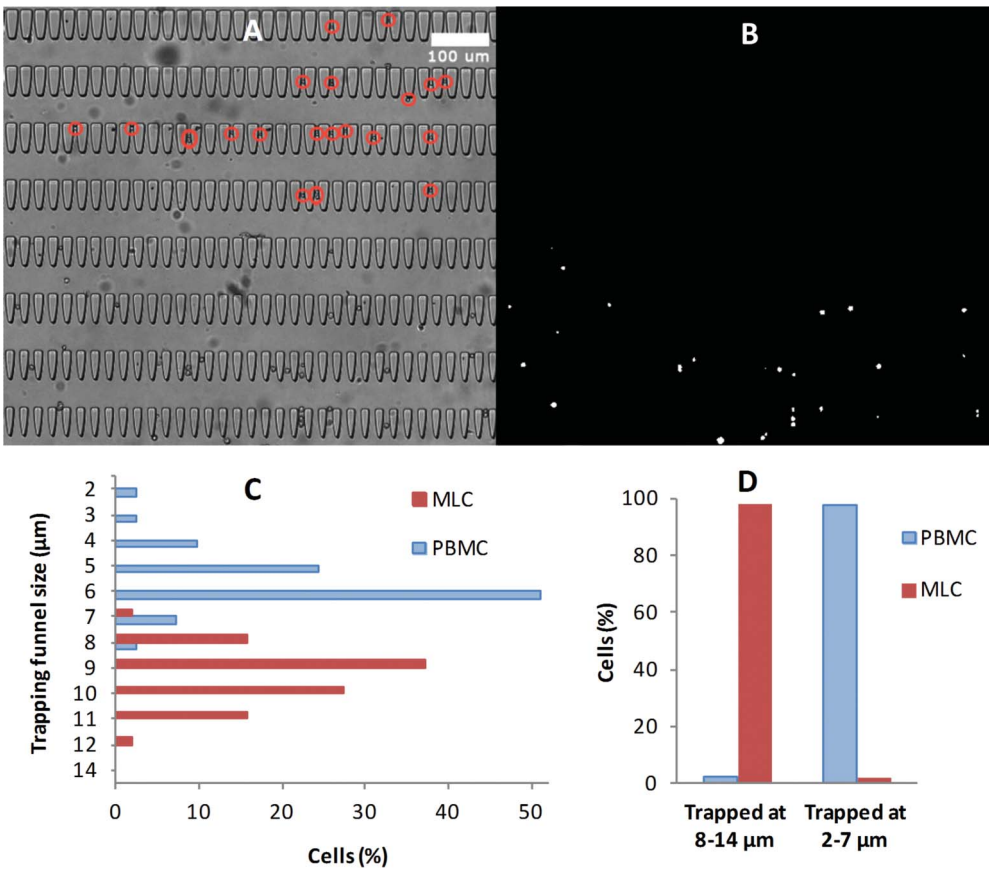

Fig. 6 Results of a cell separation experiment. (A) White light micrograph of a mixture of MLCs and PBMCs after separation. PBMCs labeled using red circles in photo. (B) Corresponding fluorescent micrograph showing the distribution of stained MLCs. (C) Resulting distribution of MLCs and PBMCs. (D) Separation efficiency and purity of the sampled cells using the 8 μm pore as a cutoff.

To determine the total number of cycles necessary to reach a steady-state distribution, we tracked the time-evolution of MLC and PBMC distributions after 0, 2, 4, 6, and 20 oscillations with oscillation pressure of 7 kPa (Fig. 7D). This pressure is the smallest used in these experiments, and will require the longest time for the cells to reach steady state due to the lower transit speed of the cells. A steady-state distribution is reached after approximately 6 oscillations for MLCs. For PBMCs, more oscillation cycles were necessary to reach a steady state distribution because of the greater distance that needed to be traversed by these cells in the device.

Ratcheting *versus* filtration

A fundamental question associated with this mechanism is whether cell separation is achieved by irreversible ratcheting or by traditional reversible filtration. To characterize the ability of our mechanism to irreversibly separate cells from the bulk liquid we evaluated the fraction of irreversibly separated cells in the following way: A sample of MLCs was first sorted using 60 s of oscillatory pressure using standard experimental parameters. Immediately following, the oscillation pressure was applied in reverse (3 s backward and 1 s forward) for another 60 s. The cells that were irreversibly separated remained trapped within their steady state positions whereas the cells that were only reversibly separated all returned to their starting position. Using an oscillation pressure of 10 kPa, over 50% of the cells were irreversibly separated. This fraction increases monotonically with increasing pressure until 100% of the cells were irreversibly separated using 41 kPa (Fig. 7E). We previously showed that ratchet transport through microscale funnel constrictions can be enabled when the applied pressure exceeds a certain threshold, dependent on cell radius and pore size.[31] Since the cell sample presents a range of cell sizes and deformabilities, increasing the applied pressure enables a greater fraction of the cells to ratchet and become irreversibly separated. While both reversible and irreversible separations are achievable using this device, operating in the irreversible regime increases the robustness of the separation for integration within automated cell processing systems.

Comparison with filtration based cell separation

The oscillatory flow and irreversible cell transport created in our mechanism improves the selectivity and scalability of traditional filtration methods. Selectivity is enhanced by the oscillatory flow, which prevents clogging, and thereby avoids altering the hydrodynamic resistance of the separation microstructure. Scalability of the separation process is enhanced because the irreversible transport of cells aids the extraction of separated cells, thereby enabling the microstructure to be refreshed for repeated separations. Compared to current filtration methods, the separation efficiency of our device is 98%, whereas other cell filtration mechanisms typically report efficiencies of 80–90%.[11,12,16] Furthermore, these studies used cultured cells from human cancer cell lines, which are larger than the MLCs used

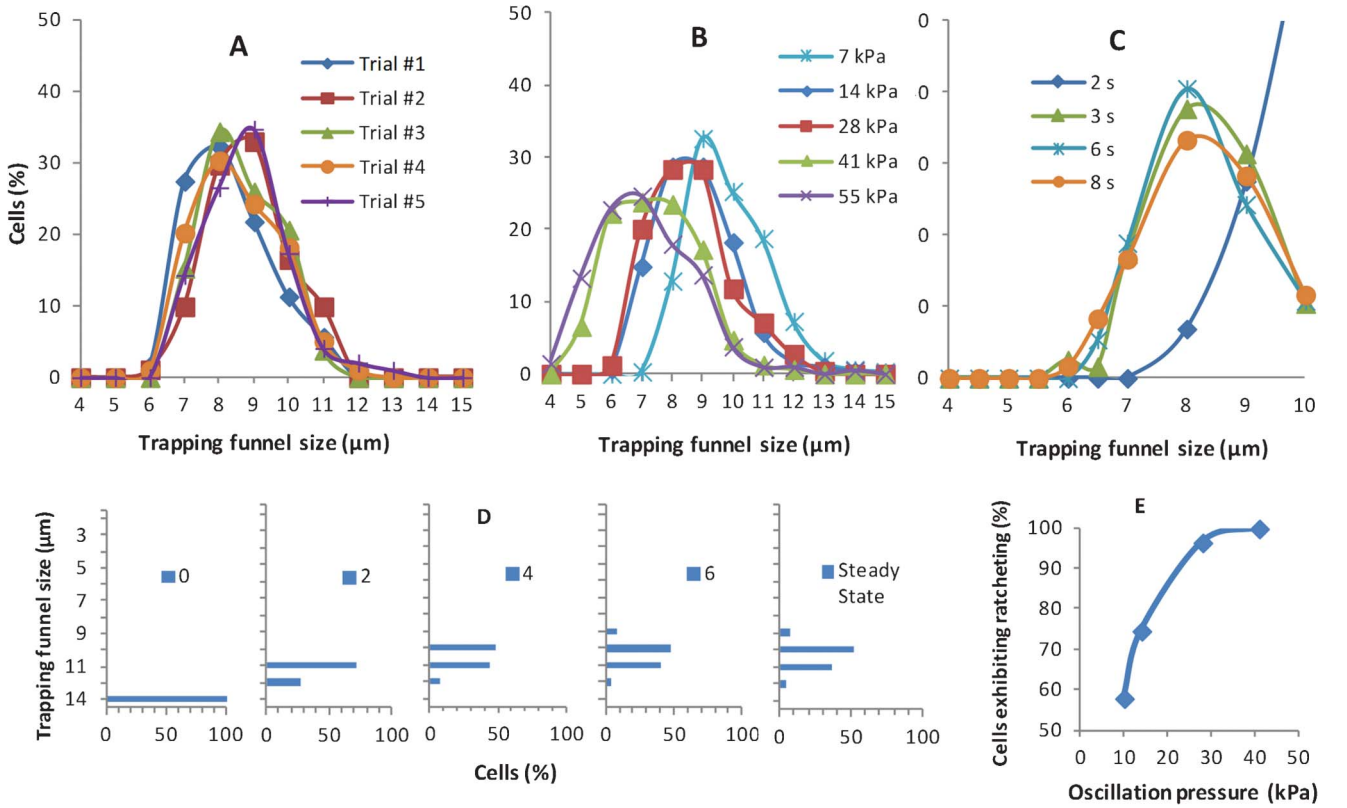

Fig. 7 Effects of experimental parameters. (A) Repeatability of MLC distributions from 5 separate trials using identical experimental parameters. (B) Effect of oscillation pressure on MLC distributions. (C) Effect of forward pressure duration on MLC distributions. (D) MLC distribution after 0, 2, 4, 6, and 20 oscillations. (E) Percentage of irreversibly separated cells as a function of oscillation pressure.

here. We demonstrated a higher efficiency using two populations of cells that are more similar in size, indicating greater selectivity. An additional advantage of our device is its ability to sort cells into multiple spatially separated regions, whereas previous mechanisms have largely been binary sorters.[9–13,15,16] In our device, multiple cell populations can be sorted simultaneously and the outlets from each sorting region can be arbitrarily grouped together to optimize for efficiency or purity, enabling this mechanism to be adapted for different cell types and applications.

Currently, we demonstrated a throughput of approximately 9000 cells per hour at standard operating conditions using a sorting area of 3200 μm × 1340 μm. We did not observe any cumulative clogging of the filter or degradation of the device functionality over continuous operation of more than 4 hours. While the throughput of this device is currently low relative to other physical separation methods, improved selectivity and scalability makes this mechanism attractive for automated sample processing systems. Methods of increasing the throughput include scaling the sorting area and increasing the speed of the oscillation flow. Ultimate applications of this mechanism may require additional pre-processing steps, such as centrifugation and negative depletion, to reduce the total number of cells in the sample prior to size and deformability based separation.

Conclusion

We used microfluidic structural ratchets arranged in a 2D array to irreversibly sort and separate cells and microparticles based on their size and deformability using oscillatory flow. The spatial distributions of sorted cells and microparticles were dependent on both size and deformability, and shown to be consistent and repeatable. This separation process is highly selective and preserves the viability of the sorted cells. We confirmed ratcheting behavior by showing that the input cells were irreversibly separated, which enabled the separated cells to be completely cleared from the separation microstructure before introducing a new batch of cells.

Acknowledgements

The authors would like to thank Elena Polishchuk, Dana Kyluik, and Mark Scott for providing materials used in this study, and Lily So and Isaac Tang for technical assistance. This work was supported by grants from the Bill and Melinda Gates Foundation, Natural Science and Engineering Research Council of Canada, Canadian Institutes of Health Research, Michael Smith Foundation for Health Research, Genome British Columbia, and the PC-TRIADD Centre of Excellence in Research and Commercialization at the Vancouver Prostate Centre.

References

1 G. Vona, C. Beroud, A. Benachi, A. Quenette, J. P. Bonnefont, S. Romana, A. Munnich, M. Vekemans, Y. Dumez, B. Lacour and P. Paterlini-Brechot, *Am. J. Pathol.*, 2002, **160**, 51–58.
2 M. Toner and D. Irimia, *Annu. Rev. Biomed. Eng.*, 2005, **7**, 77–103, DOI: 10.1146/annurev.bioeng.7.011205.135108.
3 V. Zieglschmid, C. Hollmann and O. Bocher, *Crit. Rev. Clin. Lab. Sci.*, 2005, **42**, 155–196, DOI: 10.1080/10408360590913696.
4 P. Paterlini-Brechot and N. L. Benali, *Cancer Lett.*, 2007, **253**, 180–204, DOI: 10.1016/j.canlet.2006.12.014.
5 D. Di Carlo, *Lab Chip*, 2009, **9**, 3038–3046, DOI: 10.1039/b912547g.
6 S. H. Holm, J. P. Beech, M. P. Barrett and J. O. Tegenfeldt, *Lab Chip*, 2011, **11**, 1326–1332, DOI: 10.1039/c0lc00560f.
7 L. Huang, E. Cox, R. Austin and J. Sturm, *Science*, 2004, **304**, 987–990, DOI: 10.1126/science.1094567.
8 S. C. Hur, N. K. Henderson-MacLennan, E. R. B. McCabe and D. Di Carlo, *Lab Chip*, 2011, **11**, 912–920, DOI: 10.1039/c0lc00595a.
9 H. Mohamed, M. Murray, J. N. Turner and M. Caggana, *J. Chromatogr., A*, 2009, **1216**, 8289–8295, DOI: 10.1016/j.chroma.2009.05.036.
10 S. Huang, M. Wu and G. Lee, *Sens. Actuators, B*, 2009, **142**, 389–399, DOI: 10.1016/j.snb.2009.07.046.
11 M. Hosokawa, T. Hayata, Y. Fukuda, A. Arakaki, T. Yoshino, T. Tanaka and T. Matsunaga, *Anal. Chem.*, 2010, **82**, 6629–6635, DOI: 10.1021/ac101222x.
12 S. Zheng, H. K. Lin, B. Lu, A. Williams, R. Datar, R. J. Cote and Y. Tai, *Biomed. Microdevices*, 2011, **13**, 203–213, DOI: 10.1007/s10544-010-9485-3.
13 C. Lay, C. Y. Teo, L. Zhu, X. L. Peh, H. M. Ji, B. Chew, R. Murthy, H. H. Feng and W. Liu, *Lab Chip*, 2008, **8**, 830–833, DOI: 10.1039/b800015h.
14 S. H. Seal, *Cancer*, 1964, **17**, 637.
15 H. M. Ji, V. Samper, Y. Chen, C. K. Heng, T. M. Lim and L. Yobas, *Biomed. Microdevices*, 2008, **10**, 251–257, DOI: 10.1007/s10544-007-9131-x.
16 S. J. Tan, L. Yobas, G. Y. H. Lee, C. N. Ong and C. T. Lim, *Biomed. Microdevices*, 2009, **11**, 883–892, DOI: 10.1007/s10544-009-9305-9.
17 R. Hochmuth, *J. Biomech.*, 2000, **33**, 15–22, DOI: 10.1016/S0021-9290(99)00175-X.
18 M. Rosenbluth, W. Lam and D. Fletcher, *Biophys. J.*, 2006, **90**, 2994–3003, DOI: 10.1529/biophysj.105.067496.
19 R. J. Wakeman and C. J. Williams, *Sep. Purif. Technol.*, 2002, **26**, 3–18.
20 B. Yap and R. D. Kamm, *J. Appl. Physiol.*, 2005, **99**, 2323–2330, DOI: 10.1152/japplphysiol.00503.2005.
21 X. Chen, D. F. Cui, C. C. Liu and H. Li, *Sens. Actuators, B*, 2008, **130**, 216–221, DOI: 10.1016/j.snb.2007.07.126.
22 J. S. Kuo, Y. Zhao, P. G. Schiro, L. Ng, D. S. W. Lim, J. P. Shelby and D. T. Chiu, *Lab Chip*, 2010, **10**, 837–842, DOI: 10.1039/b922301k.
23 H. Li, C. Bertram and D. Wiley, *AIChE J.*, 1998, **44**, 1950–1961, DOI: 10.1002/aic.690440903.
24 B. Q. Ai, L. Q. Wang and L. G. Liu, *Phys. Rev. E*, 2005, **72**, 031101, DOI: 10.1103/PhysRevE.72.031101.
25 A. Auge, A. Weddemann, F. Wittbracht and A. Huetten, *Appl. Phys. Lett.*, 2009, **94**, 183507, DOI: 10.1063/1.3129868.
26 S. Matthias and F. Muller, *Nature*, 2003, **424**, 53–57, DOI: 10.1038/nature01736.
27 K. Loutherback, J. Puchalla, R. H. Austin and J. C. Sturm, *Phys. Rev. Lett.*, 2009, **102**, 045301, DOI: 10.1103/PhysRevLett.102.045301.
28 A. van Oudenaarden and S. G. Boxer, *Science*, 1999, **285**, 1046–1048.
29 R. D. Astumian and P. Hanggi, *Phys. Today*, 2002, **55**, 33–39.
30 P. Haenggi and F. Marchesoni, *Rev. Mod. Phys.*, 2009, **81**, 387–442, DOI: 10.1103/RevModPhys.81.387.
31 Q. Guo, S. M. McFaul and H. Ma, *Phys. Rev. E*, 2011, **83**, 051910, DOI: 10.1103/PhysRevE.83.051910.
32 W. B. Haines, *J. Agric. Sci.*, 1930, **20**, 97–116.
33 M. A. Unger, H. P. Chou, T. Thorsen, A. Scherer and S. R. Quake, *Science*, 2000, **288**, 113–116.
34 J. Tinevez, U. Schulze, G. Salbreux, J. Roensch, J. Joanny and E. Paluch, *Proc. Natl. Acad. Sci. U. S. A.*, 2009, **106**, 18581–18586, DOI: 10.1073/pnas.0903353106.
35 R. E. Waugh and R. M. Hochmuth, in *Biomedical Engineering Fundamentals*, ed. J. D. Bronzino, CRC Press, Boca Raton, FL, 2009, pp. 474–486.

